

# Optical properties and carrier localization in the layered phosphide $\text{EuCd}_2\text{P}_2$

C. C. Homes,<sup>1,\*</sup> Z.-C. Wang,<sup>2</sup> K. Fruhling,<sup>2</sup> and F. Tafti<sup>2,†</sup>

<sup>1</sup>*National Synchrotron Light Source II, Brookhaven National Laboratory, Upton, New York 11973, USA*

<sup>2</sup>*Department of Physics, Boston College, Chestnut Hill, Massachusetts 02467, USA*

(Dated: March 23, 2023, version 2.5)

The temperature dependence of the complex optical properties of the layered phosphide material  $\text{EuCd}_2\text{P}_2$  have been measured over a wide frequency range above and below  $T_N \simeq 11.5$  K for light polarized in the  $a$ - $b$  planes. At room temperature, the optical conductivity is well described by a weak free-carrier component with a Drude plasma frequency of  $\simeq 1100$   $\text{cm}^{-1}$  and a scattering rate of  $1/\tau_D \simeq 700$   $\text{cm}^{-1}$ , with the onset of interband absorptions above  $\simeq 2000$   $\text{cm}^{-1}$ . Two infrared-active  $E_u$  modes are observed at  $\simeq 89$  and  $239$   $\text{cm}^{-1}$ . As the temperature is reduced the scattering rate decreases and the low-frequency conductivity increases slightly; however, below  $\simeq 50$  K the conductivity decreases until at the resistivity maximum at  $\simeq 18$  K (just below  $2T_N$ ) the spectral weight associated with free carriers is transferred to a localized excitation at  $\simeq 500$   $\text{cm}^{-1}$ . Below  $T_N$ , metallic behavior is recovered. Interestingly, the  $E_u$  modes are largely unaffected by these changes, with only the position of the high-frequency mode showing any signs of anomalous behavior. While several scenarios are considered, the prevailing view is that the resistivity maximum and subsequent carrier localization is due to the formation of ferromagnetic domains below  $\simeq 2T_N$  that result in spin-polarized clusters due to spin-carrier coupling [1].

PACS numbers: 63.20.-e, 78.20.-e, 78.30.-j

## I. INTRODUCTION

Magnetic semimetals display a variety of interesting phenomena. The layered europium materials  $\text{EuCd}_2X_2$ , with  $X = \text{Sb}, \text{As}, \text{and P}$ , are of particular interest as the Sb and As materials are magnetic Weyl semimetals [2–10]. These hexagonal materials have a layered crystal structure, with the  $\text{Cd}_2X_2$  layers separated by the europium layers; the magnetism originates from the europium layers which order antiferromagnetically at low temperature [11, 12]. The transport properties of these materials are intriguing as they display peaks in the resistivity close to the Néel temperature. In the case of As ( $T_N \simeq 9.5$  K), the in-plane resistivity roughly triples, while in the case of Sb ( $T_N \simeq 7.4$  K), it is more of a shoulder-like feature; however, in both cases the increase occurs at  $T_N$  and is suppressed by the application of a modest magnetic field [13]. This behavior is dramatically exaggerated in the phosphide material ( $T_N \simeq 11.5$  K). At room temperature, the in-plane resistivity may be described as that of a poor metal with  $\rho_{ab} \simeq 25$   $\text{m}\Omega \text{cm}$ ; this value increases by roughly two orders of magnitude well above  $T_N$  at  $\simeq 18$  K, effectively rendering the sample semiconducting; below this temperature the resistivity drops dramatically, falling slightly below the room temperature value at and below  $T_N$  [14]. As with Sb and As, the resistivity peak is suppressed with magnetic field, resulting in a colossal magnetoresistance. Key questions for the phosphide material are: What is the nature of the free-carrier response, and what becomes of the free-carriers at the resistivity maximum? The optical con-

ductivity is ideally suited to address these issues. The change in the dc conductivity from  $\sigma_{dc} \simeq 65$   $\Omega^{-1}\text{cm}^{-1}$  at  $\simeq 50$  K to a value that is effectively zero from an optical point of view should have a dramatic signature in the optical properties. The frequency dependence of the optical conductivity will also allow the spectral weight and the scattering rate associated with the free carriers to be determined, as well as the shifts in the spectral weight near the resistivity maximum to be tracked.

In this work the temperature dependence of the in-plane complex optical properties have been determined for a single crystal of  $\text{EuCd}_2\text{P}_2$  over a wide frequency range for light polarized in the  $a$ - $b$  planes. At room temperature, two infrared-active vibrational modes and a weak Drude-like free-carrier component are superimposed on an otherwise semiconducting response with an onset of absorption due to interband transitions at  $\gtrsim 2000$   $\text{cm}^{-1}$ . While the spectral weight associated with the free carriers remains roughly constant with decreasing temperature, the scattering rate decreases by about 10% between 295 and 50 K, consistent with the transport values for the resistivity. Below 50 K, the resistivity (and the scattering rate) increases by roughly a factor of two at 25 K, heralding the complete disappearance of the free-carrier component, the totality of which is transferred into a localized excitation centered at  $\simeq 500$   $\text{cm}^{-1}$  ( $\simeq 62$  meV); below  $T_N$  the metallic behavior is restored and the spectral weight associated with the localized excitation is transferred back into the free-carrier response. The dramatic changes in the resistivity and the optical properties are intimately connected to the magnetism in this material. While several different possibilities are considered, it appears that formation of ferromagnetic clusters at  $\simeq 2T_N$  result in carrier localization in spin-polarized clusters [1]; this effect is suppressed when the

\* homes@bnl.gov

† fazel.tafti@bc.edu

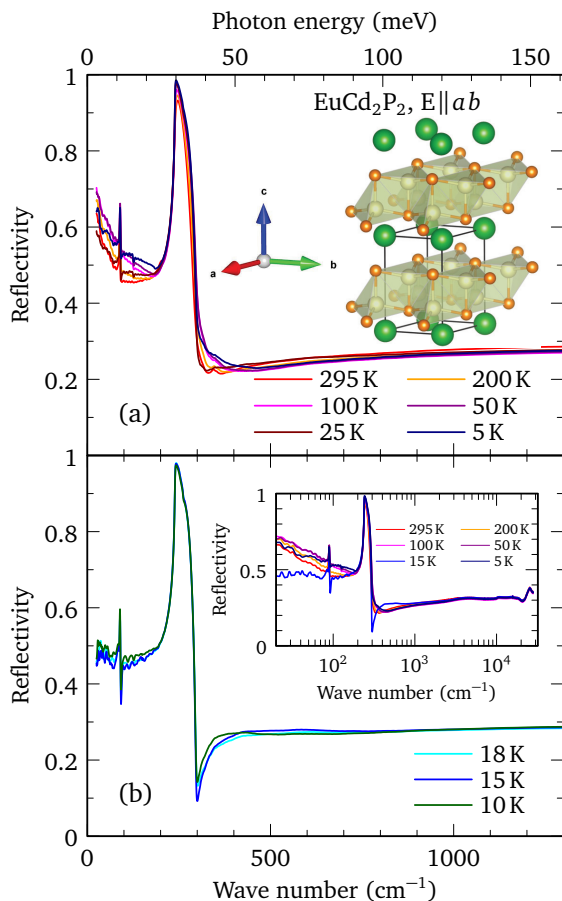


Figure 1. (a) The temperature dependence of the reflectivity of a single crystal of  $\text{EuCd}_2\text{P}_2$  versus wave number in the far-infrared region for light polarized in the  $a$ - $b$  planes for temperatures between 25 and 295 K, as well as at 5 K, where the response of the reflectivity is metallic. The resolution at low frequency is typically better than  $2 \text{ cm}^{-1}$ . Inset: the unit cell of  $\text{EuCd}_2\text{P}_2$  showing the cadmium-phosphide layers, separated by the Eu layers [15]. (b) The reflectivity between 10 and 18 K for light polarized parallel to the  $a$ - $b$  planes, where the response is now indicative of an insulating or semiconducting behavior. Inset: the reflectivity on a semi-log plot at several temperatures shown over a much wider frequency range.

clusters become contiguous and form a network. Moreover, below  $T_N$  the conductivity increases slightly, likely due to a decrease in fluctuations.

## II. EXPERIMENT AND RESULTS

Single crystals of  $\text{EuCd}_2\text{P}_2$  were grown using a flux technique that has been previously described [14]; x-ray diffraction on the large, mirror-like crystal faces revealed that they contain the  $a$ - $b$  planes. It should be noted that there is some terracing on the surface of the crystal. The reflectivity of an as-grown crystal face ( $\simeq 1.5 \text{ mm} \times 2 \text{ mm}$ ) has been measured at a near-normal angle of incidence

for light polarized parallel to the  $a$ - $b$  planes over a wide temperature and frequency range ( $\simeq 2 \text{ meV}$  to  $4 \text{ eV}$ ) using an *in situ* evaporation technique [16]; the results are shown in Fig. 1.

The character of the reflectivity may be described as either poorly metallic, or semiconducting (insulating), depending on the temperature. The response of the reflectivity is shown in the metallic case in Fig. 1(a) at temperatures between 25 and 295 K, and at 5 K; for these temperatures the low-frequency reflectivity is increasing rapidly with decreasing frequency, which is in agreement with the requirement that when  $\sigma_{dc} \neq 0$ ,  $R(\omega \rightarrow 0) = 1$ . The two prominent features in the reflectivity that are attributed to the normally infrared-active lattice modes are also partially screened [17]. In contrast, the reflectivity in Fig. 1(b) between 10 and 18 K shows a dramatically different response;  $R(\omega \rightarrow 0) \simeq \text{const}$ , the result expected for an insulator or semiconductor. In addition, the two lattice modes appear to be almost totally unscreened, resulting in fundamentally different line shapes [18].

The reflectivity is a combination of the real and imaginary parts of the dielectric function, and as such can be difficult to interpret; the real part of the optical conductivity, calculated from the imaginary part of the dielectric function, is a more intuitive quantity. Accordingly, the complex dielectric function,  $\tilde{\epsilon}(\omega) = \epsilon_1 + i\epsilon_2$ , has been determined from a Kramers-Kronig analysis of the reflectivity [19], which requires extrapolations at high and low frequency. In the case where metallic conductivity is observed, at low frequency a metallic Hagen-Rubens extrapolation,  $R(\omega) = 1 - A\sqrt{\omega}$  was employed, where  $A$  is chosen to match the value of the reflectance at the lowest measured frequency. Where an insulating or semiconducting response is observed, below the lowest measured frequency the reflectance was assumed to be constant. Above the highest-measured frequency point the reflectance was assumed to follow a  $\omega^{-1}$  dependence up to  $8 \times 10^4 \text{ cm}^{-1}$ , above which a free-electron approximation ( $R \propto \omega^{-4}$ ) was assumed [20]. The complex conductivity,  $\tilde{\sigma}(\omega) = \sigma_1 + i\sigma_2 = -2\pi i\omega[\tilde{\epsilon}(\omega) - \epsilon_\infty]/Z_0$ , where  $\epsilon_\infty$  high-frequency contribution to the real part of the dielectric function, and  $Z_0 \simeq 377 \Omega$  is the impedance of free space.

The temperature dependence of the real part of the optical conductivity for  $\text{EuCd}_2\text{P}_2$  in the low-frequency region is shown in Fig. 2 for light polarized in the  $a$ - $b$  planes. At room temperature, the optical conductivity is that of a poor metal, with  $\sigma_1(\omega \rightarrow 0) \simeq 20 \Omega^{-1}\text{cm}^{-1}$ , which is about a factor of two lower than the value obtained from transport [14]. Two sharp features, one weak and the other strong, are observed at about 89 and  $239 \text{ cm}^{-1}$ , respectively. As the temperature is reduced, the low-energy conductivity increases slightly, with  $\sigma_1(\omega \rightarrow 0) \simeq 30 \Omega^{-1}\text{cm}^{-1}$  at 50 K, which is consistent with the decreasing resistivity observed in transport [14], shown in the inset in Fig. 2. At 10, 15 and 18 K (for

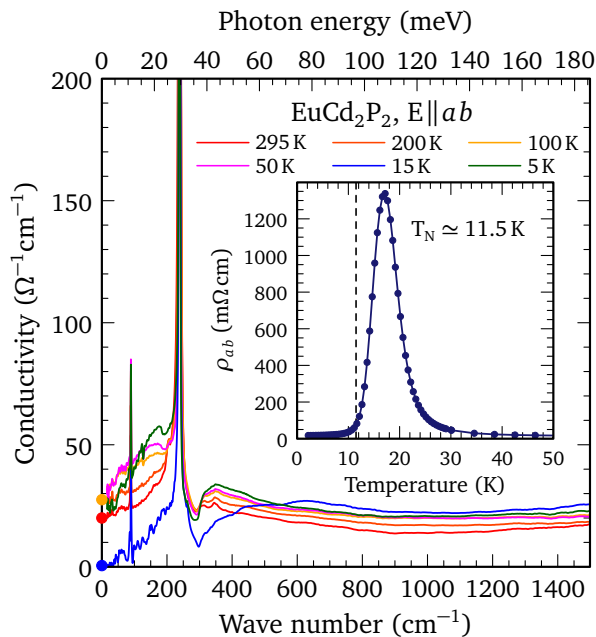


Figure 2. The temperature dependence of the real part of the optical conductivity of  $\text{EuCd}_2\text{P}_2$  versus wave number for light polarized in the  $a$ - $b$  planes in the low-frequency region. This material is a poor metal; however, at 15 K the response is semiconducting. Two sharp lattice modes are observed at  $\simeq 89$  and  $239 \text{ cm}^{-1}$ , along with a notch-like feature at about  $300 \text{ cm}^{-1}$ . The filled circles on the conductivity axis represent the extrapolated values for  $\sigma_1(\omega \rightarrow 0)$ . Inset: the temperature dependence of the  $a$ - $b$  plane dc resistivity measured in zero magnetic field. Note that the resistivity maximum occurs at  $\simeq 18 \text{ K}$ , nearly twice the value of  $T_N \simeq 11 \text{ K}$  [14].

clarity only the conductivity at 15 K is shown in Fig. 2), there is a dramatic decrease in the low-frequency conductivity, with a commensurate transfer of spectral weight (area under the conductivity curve) to high frequency, leading to an increase in the optical conductivity above  $\simeq 600 \text{ cm}^{-1}$ . Interestingly, below  $T_N$  at 5 K the metallic behavior is recovered and spectral weight is transferred back into the free-carrier component.

### III. DISCUSSION

To investigate the behavior of the free-carriers in more detail, the optical response has been modeled using the Drude-Lorentz model for the complex dielectric function

$$\tilde{\epsilon}(\omega) = \epsilon_\infty - \frac{\omega_{p,D}^2}{\omega^2 + i\omega/\tau_D} + \sum_j \frac{\Omega_j^2}{\omega_j^2 - \omega^2 - i\omega\gamma_j}. \quad (1)$$

In the first term  $\omega_{p,D}^2 = 4\pi n e^2/m^*$  and  $1/\tau_D$  are the square of the plasma frequency and scattering rate for the delocalized (Drude) carriers, respectively, and  $n$  and  $m^*$  are the carrier concentration and effective mass. In the summation,  $\omega_j$ ,  $\gamma_j$  and  $\Omega_j$  are the position, width,

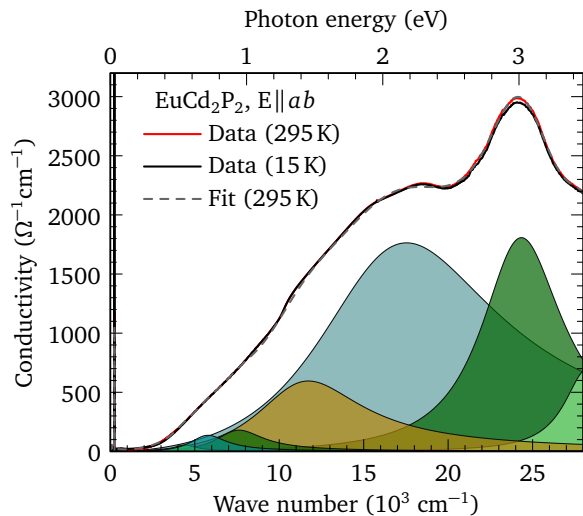


Figure 3. The optical conductivity of  $\text{EuCd}_2\text{P}_2$  at 295 and 15 K for light polarized in the  $a$ - $b$  planes over a wide frequency range, showing the onset of absorption due to interband transitions at  $\simeq 2000 \text{ cm}^{-1}$ , and the lack of any strong temperature dependence in this region. The result of the fit to the optical conductivity of  $\text{EuCd}_2\text{P}_2$  at 295 K using the Drude-Lorentz mode is indicated by the dashed line; the fit is decomposed into the contributions from the different Lorentz oscillators.

and strength of a symmetric Lorentzian oscillator that describe the  $j$ th vibration or bound excitation.

The strategy that we will adopt in fitting the optical conductivity is to first fit the interband transitions to Lorentzian oscillators using a non-linear least squares technique, then, either holding these high-frequency oscillators fixed or allowing only modest refinement, fit the free-carrier response in the low-frequency region. The general approach is to use the minimum number of oscillators required to describe the data. The real part of the in-plane optical conductivity is shown over a wide frequency range at several temperatures in Fig. 3, showing the onset of absorption above  $\simeq 2000 \text{ cm}^{-1}$ , along with the results of the fit at 295 K. Oscillators have been introduced at  $\simeq 0.54, 0.71, 0.95, 1.45, 2.17, 3.02,$  and  $3.50 \text{ eV}$ ; the fit has been decomposed into the contributions from the Lorentz oscillators. While the overall fit is excellent, it can be argued that the low-frequency oscillator could probably be removed and a reasonable fit still obtained; however, the low-frequency oscillator is required to reproduce the linear region of the optical conductivity, which then allows the low-frequency conductivity to be fit reliably. We also note that because the oscillator at  $3.5 \text{ eV}$  is at the limit of the measured data, it should be treated with caution.

The determination of the frequencies for the interband transitions allows the low-frequency conductivity to be fit using the Drude model. However, the sharp features attributed to the lattice modes complicate this approach; it is simpler to fit these features and then subtract them

from the conductivity, leaving only the electronic continuum associated with the free carriers. Accordingly, the rest of the discussion will first deal with the vibrational properties, followed by an analysis of the free-carrier response.

### A. Vibrational properties

In the hexagonal (trigonal)  $P\bar{3}m1$  setting, the irreducible vibrational representation for  $\text{EuCd}_2\text{P}_2$  is  $\Gamma_{\text{irr}} = 2A_{1g} + 2E_g + 2A_{2u} + 2E_u$ . The  $A_{1g}$  and  $E_g$  modes are Raman active, while the  $A_{2u}$  and  $E_u$  modes are infrared active along the  $c$  axis and the  $a$ - $b$  planes, respectively. The two modes observed in Fig. 2 at  $\simeq 89$  and  $239 \text{ cm}^{-1}$  are the expected  $E_u$  modes. It is tempting to assume that the notch-like feature just above the high-frequency mode at  $\simeq 300 \text{ cm}^{-1}$  is due to electron-phonon coupling resulting in a Fano-like antiresonance in the electronic continuum [21, 22]. However, it should be noted that this vibration is exceptionally strong and narrow; it does not show the broadening that would be expected for a mode that was coupled to the electronic background [23]. Moreover, there is almost no electronic background for it to interact with. The low-frequency mode also displays no sign of any asymmetry. The two modes have therefore been fit using a symmetric Lorentzian on a linear background. The results of the fits to the two  $E_u$  mode are shown in Fig. 4.

The temperature dependence of the position of the low-energy  $E_u$  mode, shown in Fig. 4(a), behaves in the expected way, increasing in frequency (hardening) with decreasing temperature from  $\simeq 88$  to about  $89.5 \text{ cm}^{-1}$  at low temperature. At room temperature this mode is quite narrow with a line width of  $\simeq 2 \text{ cm}^{-1}$ , and it decreases only slightly to  $1.7 \text{ cm}^{-1}$  at low temperature; the oscillator strength is roughly constant with  $\Omega_0 \simeq 68 \text{ cm}^{-1}$ . Overall, this behavior is what is expected for a symmetric anharmonic decay of an optic mode into two acoustic modes with identical frequencies and opposite momenta [24, 25]. The functional form employed here is,

$$\omega_0(T) = \omega_B \left[ 1 - \frac{2C}{e^x - 1} \right], \quad (2)$$

$$\gamma_0(T) = \Gamma_0 \left[ 1 + \frac{2\Gamma}{e^x - 1} \right], \quad (3)$$

where  $\omega_B$  is the bare phonon frequency,  $\Gamma_0$  is a residual line width,  $C$  and  $\Gamma$  are constants, and  $x = \hbar\omega_B/(2k_B T)$ ; the bare phonon frequency (residual line width) is recovered in the  $T \rightarrow 0$  limit [26]. The model fits are indicated by the dashed lines in Figs. 4(a) and 4(b).

In contrast, the frequency dependence of the high-frequency  $E_u$  mode, shown in Fig. 4(d), is somewhat anomalous, initially hardening with decreasing temperature, reaching a maximum of  $\simeq 239.5 \text{ cm}^{-1}$  at  $100 \text{ K}$

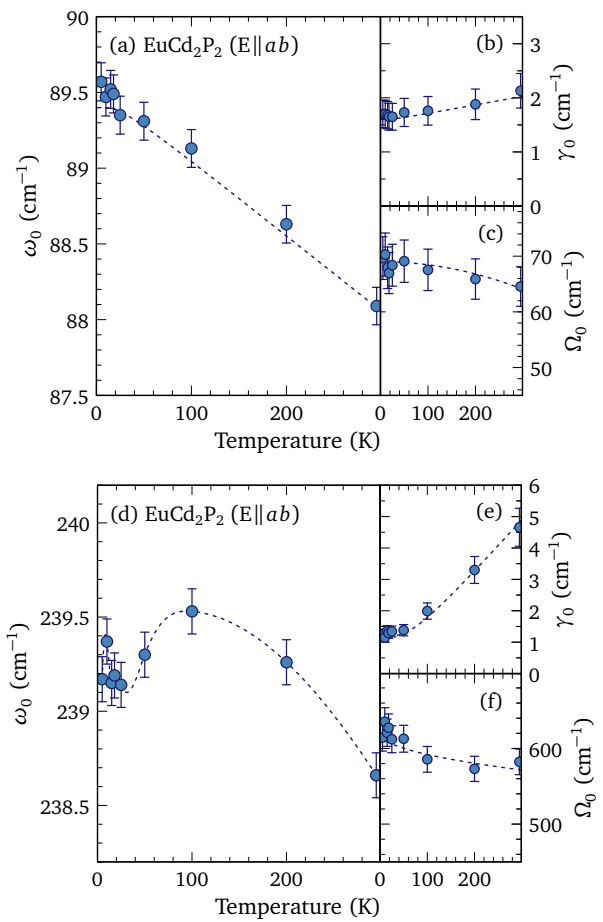


Figure 4. The results of the fit to the  $-n$ -plane optical conductivity using symmetric Lorentzian oscillators for the  $E_u$  modes in  $\text{EuCd}_2\text{P}_2$ . The upper panel shows the temperature dependence of (a) the position, (b) line width, and (c) strength of the low-frequency  $E_u$  mode; the dashed lines for the position and line width are calculated using the anharmonic decay model using  $\omega_B = 89.5 \text{ cm}^{-1}$  ( $C = 0.0019$ ), and  $\gamma_0 = 1.6 \text{ cm}^{-1}$  ( $\Gamma = 0.032$ ), respectively. The lower panel shows the (d) the position, (e) line width, and (f) strength of the high-frequency  $E_u$  mode. The dashed line for the line width is generated using the anharmonic decay model with  $\gamma_0 = 1.2 \text{ cm}^{-1}$  ( $\Gamma = 1.32$ ); all others are drawn as a guide to the eye.

before softening by nearly  $1 \text{ cm}^{-1}$  as the temperature continues to decrease, then hardening again below about  $25 \text{ K}$ , suggesting a weak coupling to the magnetism in this material. Surprisingly, this mode narrows from  $\simeq 5$  to  $1.3 \text{ cm}^{-1}$  at low temperature in a uniform way, as shown in Fig. 4(e), and can be described by the anharmonic decay model, showing none of the anomalous behavior observed in the position, although there is some evidence the oscillator strength of this mode may increase slightly at low temperature, shown in Fig. 4(f).

The optical conductivity the fits were performed on have a typical wave number resolution of  $1.8 \text{ cm}^{-1}$ . Measurements with a resolution of  $0.2 \text{ cm}^{-1}$  were performed

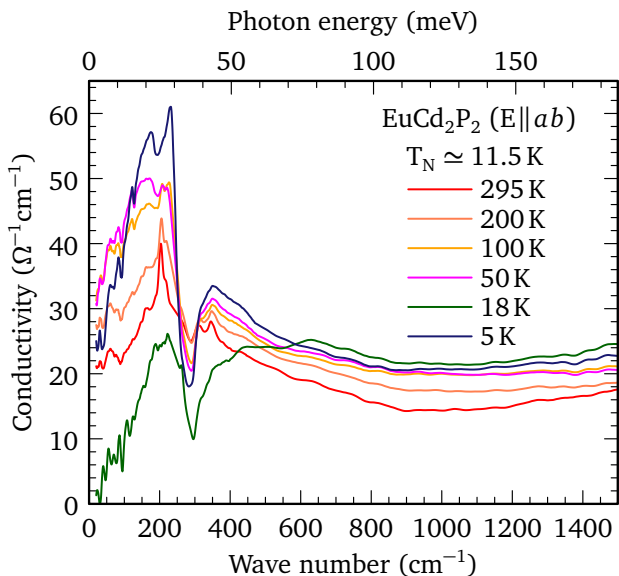


Figure 5. The temperature dependence of the optical conductivity of  $\text{EuCd}_2\text{P}_2$  for light polarized in the  $a$ - $b$  planes in the far-infrared region with the infrared-active  $E_u$  modes removed, revealing the non-Drude response.

in the far-infrared region above and below  $T_N$  revealed that while the two modes have the same positions as previously reported, the line width of the low-frequency mode of  $\simeq 0.2 \text{ cm}^{-1}$  suggests it is limited by the resolution of the instrument, while the high-frequency mode has a width of  $0.53 \text{ cm}^{-1}$ , indicating that this is likely its intrinsic value [18]. Interestingly, neither mode splits below  $T_N$ , suggesting the antiferromagnetic ground state does not result in a significant lattice distortion.

### B. Electronic response

The determination of the vibrational parameters for the two  $E_u$  modes allows these features to be subtracted from the optical conductivity in Fig. 2, resulting in the residual conductivity shown in Fig. 5. There are several things about the residual conductivity that are unusual. The first is that the conductivity is non-Drude; it is initially increasing as a function of frequency, reaching a maximum at  $\simeq 200 \text{ cm}^{-1}$  before encountering a notch-like feature between  $250\text{--}300 \text{ cm}^{-1}$ . The Drude form for the real part of the optical conductivity may be written as

$$\sigma_1(\omega) = \left( \frac{2\pi}{Z_0} \right) \frac{\omega_{p,D}^2 \tau_D}{1 + \omega^2 \tau_D^2}, \quad (4)$$

which has the form of a Lorentzian centered at zero frequency with a width of  $1/\tau_D$ .

The origin of the notch-like feature may arise from the terraced nature of the crystal surface, which can introduce structure from the  $c$  axis into the  $ab$ -plane optical

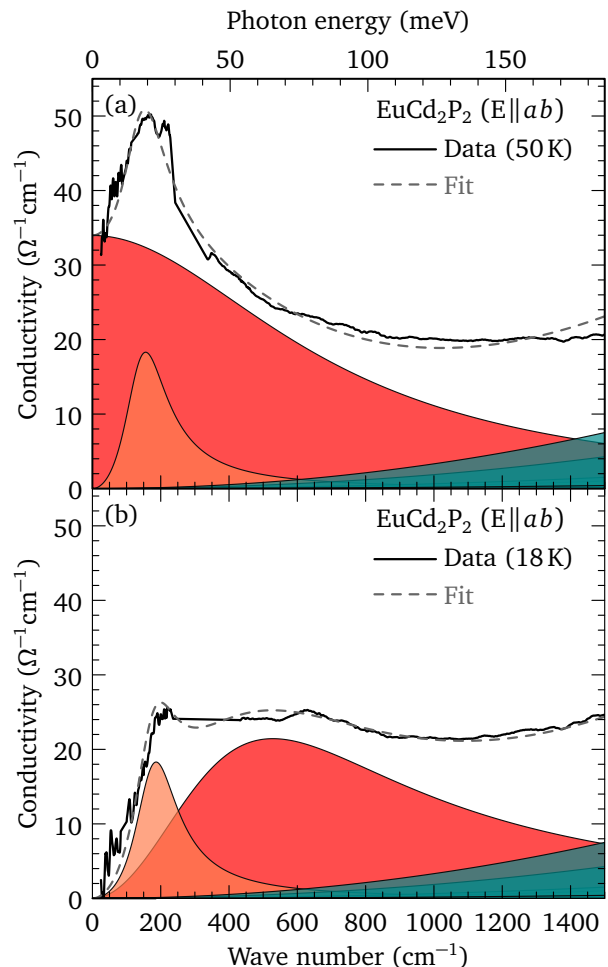


Figure 6. The fit using the Drude-Lorentz model to the real part of the optical conductivity of  $\text{EuCd}_2\text{P}_2$  for light polarized in the  $a$ - $b$  planes with the infrared-active  $E_u$  modes and the notch-like feature removed at (a) 50 K, and (b) 18 K. The fit has been decomposed into the contributions for the free-carrier response as well as the bound excitations. The spectral weight associated with the Drude component is observed to shift to a bound excitation (red curve) with a weaker component that does not change, while the darker colors indicate the low-frequency tails of the mid-infrared absorptions.

properties. Alternatively, it has been established that in anisotropic media such as the cuprate materials, measuring the reflectivity at anything other than a normal angle of incidence, or having a slightly misoriented surface, can allow  $c$ -axis longitudinal optic (LO) modes to manifest themselves as antiresonances (resonances) in the metallic (insulating) electronic background [27–29]. The results from an  $a$ - $c$  [(101)] face allows the positions of the  $A_{2u}$  transverse optic (TO) modes to be determined and the lower bound of the LO modes to be estimated; comparison with the in-plane results reveal that the artifacts in the  $a$ - $b$  plane reflectivity arise from the  $c$  axis TO modes. The terraces lead to a mixing of the in-plane and  $c$  axis reflectivity, thus the notch-like feature is considered to

Table I. The fitted values for the residual optical conductivity of  $\text{EuCd}_2\text{P}_2$  for light polarized in the  $a$ - $b$  planes, consisting of Drude parameters in the metallic state, and a bound excitation in the semiconducting state; the estimated error on the fitted quantities is approximately 10%. All units are in  $\text{cm}^{-1}$ , unless otherwise indicated.

| $T$ (K) | $\omega_{p,D}$ | $1/\tau_D$ | $\omega_0$ | $\gamma_0$ | $\Omega_0$ |
|---------|----------------|------------|------------|------------|------------|
| 295     | 993            | 756        |            |            |            |
| 200     | 1100           | 753        |            |            |            |
| 100     | 1160           | 680        |            |            |            |
| 50      | 1193           | 698        |            |            |            |
| 25      | 1311           | 1265       |            |            |            |
| 18      |                |            | 486        | 1180       | 1183       |
| 15      |                |            | 539        | 1028       | 1154       |
| 10      |                |            | 426        | 770        | 1078       |
| 5       | 1170           | 919        |            |            |            |

<sup>a</sup> A low-frequency bound excitation is also included at all temperatures to describe the low-frequency conductivity; while it's parameters vary,  $\omega_0 \approx \gamma_0 \simeq 180 \text{ cm}^{-1}$ , and  $\Omega_0 \simeq 400 \text{ cm}^{-1}$ , except at 5 K where it increases to  $\simeq 600 \text{ cm}^{-1}$ .

be an artifact and not intrinsic and will be ignored in fits to the residual conductivity; this is discussed in detail in the Supplementary Materials [18].

The residual optical conductivity has been fit using the Drude-Lorentz model and the results for two representative fits at 50 and 18 K are shown in Figs. 6(a) and 6(b), respectively; the bound excitations associated with the interband transitions have been held fixed, partly to allow for a more reliable convergence, and also because little temperature dependence of these features is expected (Fig. 3). The quality of the fits are quite good. In the metallic state at 50 K, the Drude response dominates the free-carrier response with  $\omega_{p,D} \simeq 1200 \text{ cm}^{-1}$  with a scattering rate of  $1/\tau_D \simeq 700 \text{ cm}^{-1}$ , values that are representative of a marginally-metallic material. A weak bound excitation at  $\simeq 180 \text{ cm}^{-1}$  has been included to reproduce the non-Drude response at low frequency; however, it represents only about 10% of the spectral weight associated with the free carriers. At 18 K, the Drude response vanishes and essentially all of the spectral weight associated with free carriers has been transferred to a bound excitation at  $\omega_0 \simeq 500 \text{ cm}^{-1}$ , with a width  $\gamma_0 \simeq 1200 \text{ cm}^{-1}$  and  $\Omega_0 \simeq 1200 \text{ cm}^{-1}$ . The results of the fits have been summarized in Table I. While position of the excitation at  $\simeq 180 \text{ cm}^{-1}$  shows little temperature dependence, it does increase somewhat in strength below  $T_N$ , suggesting that it is affected by the formation of magnetic order; however, its origin remains unclear.

The temperature dependence of Drude plasma frequency is roughly constant with a value of  $\omega_{p,D} \simeq 1150 \pm 150 \text{ cm}^{-1}$ . When the Drude term vanishes at temperatures close to the resistivity maximum, the free-carrier spectral weight is transferred into a localized excitation with  $\Omega_0 \simeq \omega_{p,D}$ , which is also temperature independent. On the other hand, the Drude scattering rate decreases from  $1/\tau_D \simeq 760$  to  $700 \text{ cm}^{-1}$  at 50 K, but

then increases dramatically at 25 K, just above the resistivity maximum, to  $1/\tau_D \simeq 1270 \text{ cm}^{-1}$ . It is tempting to associate the rapid increase in  $1/\tau_D$  close to  $T_N$  with the scattering of carriers from antiferromagnetic fluctuations. This argument would be reasonable if the maximum in the resistivity occurred just above  $T_N$ ; however, it occurs at  $\simeq 18 \text{ K}$ , nearly twice  $T_N$ . Moreover, the resistivity in this material increases by roughly two orders of magnitude, far greater than the modest increases that are observed at  $\simeq T_N$  in the As and Sb compounds.

A more conventional approach relies on polaron effects to describe the transport behavior in the colossal magnetoresistance materials [30–35]. For instance, a transition from large (delocalized carriers) to small polarons (localized carriers) has been used to explain the metal-insulator transition in manganites [36, 37]. The application of polarons to this material is attractive because the shape of the electronic absorption is that of an asymmetric Gaussian with a long high-frequency tail [37], which it could be argued better describes the electronic background in Fig. 6(b) than the two Lorentzian oscillators; additionally, the peak of the localized carriers occurs at  $\simeq 480 \pm 50 \text{ cm}^{-1}$ , which is roughly twice the energy of the high-frequency  $E_u$  mode, consistent with a polaronic mechanism. There are several problems with this interpretation. The first is that small lattice polarons are expected to form in systems with strong electron-phonon coupling [35]; however, as previously noted, the narrow line shapes of the infrared-active  $E_u$  modes do not support the notion of strong electron-phonon coupling. Additionally, the size of this effect is orders of magnitude smaller than what is observed in the manganites, and finally, no removal of degeneracy due to the coupling of the infrared-active modes to a lattice distortion is observed. Consequently, the polaronic view is not favored.

The most compelling explanation for the dramatic increase of the resistivity above  $T_N$  lies in the recent observation of the formation of ferromagnetism at  $\simeq 2T_N$  [1]; ferromagnetic clusters form in a paramagnetic background, resulting in carriers becoming localized into spin-polarized clusters due to spin-carrier coupling. Optically, this is observed as the transfer of spectral weight from the free-carriers into a localization peak. The resistivity continues to increase until the ferromagnetic regions begin to merge into a contiguous network just above  $T_N$ , at which point the resistivity begins to decrease and the spectral weight is transferred back into the free-carrier component. The ferromagnetic regions are observed to persist below  $T_N$  in the metallic antiferromagnetic phase where the conductivity has improved slightly, likely due to a decrease in spin fluctuations [38].

#### IV. CONCLUSIONS

The optical properties of a single crystal of  $\text{EuCd}_2\text{P}_2$  have been determined for light polarized in the  $a$ - $b$  planes above and below  $T_N$  over a wide frequency range. At

room temperature, the real part of the optical conductivity reveals a marginally-metallic material, consisting of a weak free-carrier component with the onset of interband transitions above  $\simeq 2000 \text{ cm}^{-1}$ . Two sharp infrared-active  $E_u$  modes are observed at  $\simeq 89$  and  $239 \text{ cm}^{-1}$ . In addition, a spurious notch-like feature observed in the in-plane conductivity is attributed to  $c$ -axis contamination due to terraces in the crystal surface [18]. As the temperature is lowered, there is a modest increase in the low-frequency conductivity; however, below about 50 K the conductivity begins to decrease until at  $\simeq 18 \text{ K}$  (just below  $2T_N$ ), a dramatic change is observed as the majority of the free-carriers enter into a localized state, before reverting back to metallic behavior again below  $T_N$ . The loss and subsequent restoration of the free-carrier electronic background has a relatively minor effect on the nature of the  $E_u$  modes; however, it results in a dramatic change in the line shapes of these vibrations in the reflectivity [18]. The localization of the free carriers is

intimately connected with the magnetism in this material. While several scenarios are considered, the prevailing explanation for the resistivity maximum and carrier localization is the formation of ferromagnetic domains below  $\simeq 2T_N$  that result in spin-polarized clusters due to spin-carrier coupling; once these domains form a contiguous network, the resistivity decreases and the free-carrier component is restored [1].

## ACKNOWLEDGMENTS

We would like to acknowledge useful discussions with A. Akrap, V. Sunko and J. Orenstein. The work at Boston College was funded by the National Science Foundation under Award No. NSF/DMR-1708929. Work at Brookhaven National Laboratory was supported by the Office of Science, U.S. Department of Energy under Contract No. DE-SC0012704.

- 
- [1] V. Sunko, Y. S. M. Vranas, C. C. Homes, C. Lee, E. Donoway, Z.-C. Wang, S. Balguri, M. B. Mahendru, A. Ruiz, B. Gunn, R. Basak, E. Schierle, E. Weschke, F. Tafti, A. Frano, and J. Orenstein, Spin-carrier coupling induced ferromagnetism and giant resistivity peak in  $\text{EuCd}_2\text{P}_2$ , [arXiv:2208.05499v1](#) (2022).
- [2] H. P. Wang, D. S. Wu, Y. G. Shi, and N. L. Wang, Anisotropic transport and optical spectroscopy study on antiferromagnetic triangular lattice  $\text{EuCd}_2\text{As}_2$ : An interplay between magnetism and charge transport properties, *Phys. Rev. B* **94**, 045112 (2016).
- [3] J.-Z. Ma, S. M. Nie, C. J. Yi, J. Jandke, T. Shang, M. Y. Yao, M. Naamneh, L. Q. Yan, Y. Sun, A. Chikina, V. N. Strocov, M. Medarde, M. Song, Y.-M. Xiong, G. Xu, W. Wulfhekel, J. Mesot, M. Reticcioli, C. Franchini, C. Mudry, M. Müller, Y. G. Shi, T. Qian, H. Ding, and M. Shi, Spin fluctuation induced Weyl semimetal state in the paramagnetic phase of  $\text{EuCd}_2\text{As}_2$ , *Sci. Adv.* **5**, eaaw4718 (2019).
- [4] L.-L. Wang, N. H. Jo, B. Kuthanazhi, Y. Wu, R. J. McQueeney, A. Kaminski, and P. C. Canfield, Single pair of Weyl fermions in the half-metallic semimetal  $\text{EuCd}_2\text{As}_2$ , *Phys. Rev. B* **99**, 245147 (2019).
- [5] J. Behrends, R. Ilan, and J. H. Bardarson, Anomalous conductance scaling in strained Weyl semimetals, *Phys. Rev. Research* **1**, 032028 (2019).
- [6] J.-R. Soh, F. de Juan, M. G. Vergniory, N. B. M. Schröter, M. C. Rahn, D. Y. Yan, J. Jiang, M. Bristow, P. Reiss, J. N. Blandy, Y. F. Guo, Y. G. Shi, T. K. Kim, A. McCollam, S. H. Simon, Y. Chen, A. I. Coldea, and A. T. Boothroyd, Ideal Weyl semimetal induced by magnetic exchange, *Phys. Rev. B* **100**, 201102 (2019).
- [7] N. H. Jo, B. Kuthanazhi, Y. Wu, E. Timmons, T.-H. Kim, L. Zhou, L.-L. Wang, B. G. Ueland, A. Palasyuk, D. H. Ryan, R. J. McQueeney, K. Lee, B. Schrunck, A. A. Burkov, R. Prozorov, S. L. Bud'ko, A. Kaminski, and P. C. Canfield, Manipulating magnetism in the topological semimetal  $\text{EuCd}_2\text{As}_2$ , *Phys. Rev. B* **101**, 140402(R) (2020).
- [8] H. Su, B. Gong, W. Shi, H. Yang, H. Wang, W. Xia, Z. Yu, P.-J. Guo, J. Wang, L. Ding, L. Xu, X. Li, X. Wang, Z. Zou, N. Yu, Z. Zhu, Y. Chen, Z. Liu, K. Liu, G. Li, and Y. Guo, Magnetic exchange induced Weyl state in a semimetal  $\text{EuCd}_2\text{Sb}_2$ , *APL Materials* **8**, 011109 (2020).
- [9] J. Ma, H. Wang, S. Nie, C. Yi, Y. Xu, H. Li, J. Jandke, W. Wulfhekel, Y. Huang, D. West, P. Richard, A. Chikina, V. N. Strocov, J. Mesot, H. Weng, S. Zhang, Y. Shi, T. Qian, M. Shi, and H. Ding, Emergence of Non-trivial Low-Energy Dirac Fermions in Antiferromagnetic  $\text{EuCd}_2\text{As}_2$ , *Adv. Mater.* **32**, 1907565 (2020).
- [10] Y. Xu, L. Das, J. Z. Ma, C. J. Yi, S. M. Nie, Y. G. Shi, A. Tiwari, S. S. Tsirkin, T. Neupert, M. Medarde, M. Shi, J. Chang, and T. Shang, Unconventional Transverse Transport above and below the Magnetic Transition Temperature in Weyl Semimetal  $\text{EuCd}_2\text{As}_2$ , *Phys. Rev. Lett.* **126**, 076602 (2021).
- [11] I. Schellenberg, U. Pfannenschmidt, M. Eul, C. Schwickert, and R. Pöttgen, A  $^{121}\text{Sb}$  and  $^{151}\text{Eu}$  Mössbauer Spectroscopic Investigation of  $\text{EuCd}_2\text{X}_2$  ( $X = \text{P}, \text{As}, \text{Sb}$ ) and  $\text{YbCd}_2\text{Sb}_2$ , *Z. Anorg. Allg. Chem.* **637**, 1863 (2011).
- [12] M. C. Rahn, J.-R. Soh, S. Francoual, L. S. I. Veiga, J. Strempler, J. Mardegan, D. Y. Yan, Y. F. Guo, Y. G. Shi, and A. T. Boothroyd, Coupling of magnetic order and charge transport in the candidate Dirac semimetal  $\text{EuCd}_2\text{As}_2$ , *Phys. Rev. B* **97**, 214422 (2018).
- [13] J.-R. Soh, E. Schierle, D. Y. Yan, H. Su, D. Prabhakaran, E. Weschke, Y. F. Guo, Y. G. Shi, and A. T. Boothroyd, Resonant x-ray scattering study of diffuse magnetic scattering from the topological semimetals  $\text{EuCd}_2\text{As}_2$  and  $\text{EuCd}_2\text{Sb}_2$ , *Phys. Rev. B* **102**, 014408 (2020).
- [14] Z.-C. Wang, J. D. Rogers, X. Yao, R. Nichols, K. Atay, B. Xu, J. Franklin, I. Sochnikov, P. J. Ryan, D. Haskel, and F. Tafti, Colossal magnetoresistance without mixed valence in a layered phosphide crystal, *Adv. Mater.* **33**, 2005755 (2021).

- [15] K. Momma and F. Izumi, *VESTA 3* for three-dimensional visualization of crystal, volumetric and morphology data, *J. Appl. Cryst.* **44**, 1272 (2011).
- [16] C. C. Homes, M. Reedyk, D. A. Crandles, and T. Timusk, Technique for measuring the reflectance of irregular, submillimeter-sized samples, *Appl. Opt.* **32**, 2976 (1993).
- [17] C. C. Homes, A. W. McConnell, B. P. Clayman, D. A. Bonn, R. Liang, W. N. Hardy, M. Inoue, H. Negishi, P. Fournier, and R. L. Greene, Phonon Screening in High-Temperature Superconductors, *Phys. Rev. Lett.* **84**, 5391 (2000).
- [18] See Supplemental Material at [URL will be inserted by publisher] for a discussion of how a weak electronic background can fundamentally alter the vibrational line shape in the reflectivity. Examples of terracing in  $\text{EuCd}_2\text{P}_2$  are shown; the experimental high-resolution ( $0.2 \text{ cm}^{-1}$ ) in-plane [(001)] reflectivity, as well as the reflectivity from an  $a$ - $c$  [(101)] face is shown. The fitted values of the in-plane  $E_u$  and  $c$ -axis  $A_{2u}$  modes, as well as estimates for the positions of the LO modes, are presented; estimates of  $\epsilon_\infty$  are validated by examining the positions of the  $a$ - $b$  plane TO and LO modes. The analysis concludes that terracing leads to artifacts in the reflectivity due to the simple mixing of the  $a$ - $b$  plane and  $c$  axis reflectivity.
- [19] M. Dressel and G. Grüner, *Electrodynamics of Solids* (Cambridge University Press, Cambridge, 2001).
- [20] F. Wooten, *Optical Properties of Solids* (Academic Press, New York, 1972) pp. 244–250.
- [21] U. Fano, Effects of configuration interaction on intensities and phase shifts, *Phys. Rev.* **124**, 1866 (1961).
- [22] A. Damascelli, *Optical Spectroscopy of Quantum Spin Systems*, Ph.D. thesis, University of Groningen (1996), p. 21.
- [23] Y. Wang, L. Rademaker, E. Dagotto, and S. Johnston, Phonon linewidth due to electron-phonon interactions with strong forward scattering in FeSe thin films on oxide substrates, *Phys. Rev. B* **96**, 054515 (2017).
- [24] P. G. Klemens, Anharmonic decay of optical phonons, *Phys. Rev.* **148**, 845 (1966).
- [25] J. Menéndez and M. Cardona, Temperature dependence of the first-order Raman scattering by phonons in Si, Ge, and  $\alpha$ -Sn: Anharmonic effects, *Phys. Rev. B* **29**, 2051 (1984).
- [26] C. C. Homes, Y. M. Dai, J. Schneeloch, R. D. Zhong, and G. D. Gu, Phonon anomalies in some iron telluride materials, *Phys. Rev. B* **93**, 125135 (2016).
- [27] D. W. Berreman, Resonant Reflectance Anomalies: Effect of Shapes of Surface Irregularities, *Phys. Rev. B* **1**, 381 (1970).
- [28] M. Reedyk and T. Timusk, Evidence for  $a$ - $b$ -plane coupling to longitudinal  $c$ -axis phonons in high- $T_c$  superconductors, *Phys. Rev. Lett.* **69**, 2705 (1992).
- [29] C. C. Homes, J. M. Tranquada, and D. J. Buttrey, Stripe order and vibrational properties of  $\text{La}_2\text{NiO}_{4+\delta}$  for  $\delta = 2/15$ : Measurements and *ab initio* calculations, *Phys. Rev. B* **75**, 045128 (2007).
- [30] D. Emin, Optical properties of large and small polarons and bipolarons, *Phys. Rev. B* **48**, 13691 (1993).
- [31] A. S. Alexandrov and N. Mott, *Polarons & Bipolarons* (World Scientific, Cambridge, 1995).
- [32] A. J. Millis, R. Mueller, and B. I. Shraiman, Fermi-liquid-to-polaron crossover. II. Double exchange and the physics of colossal magnetoresistance, *Phys. Rev. B* **54**, 5405 (1996).
- [33] H. Röder, J. Zang, and A. R. Bishop, Lattice Effects in the Colossal-Magnetoresistance Manganites, *Phys. Rev. Lett.* **76**, 1356 (1996).
- [34] J. D. Lee and B. I. Min, Polaron transport and lattice dynamics in colossal-magnetoresistance manganites, *Phys. Rev. B* **55**, 12454 (1997).
- [35] M. B. Salamon and M. Jaime, The physics of manganites: Structure and transport, *Rev. Mod. Phys.* **73**, 583 (2001).
- [36] A. Lanzara, N. L. Saini, M. Brunelli, F. Natali, A. Bianconi, P. G. Radaelli, and S.-W. Cheong, Crossover from Large to Small Polarons across the Metal-Insulator Transition in Manganites, *Phys. Rev. Lett.* **81**, 878 (1998).
- [37] C. Hartinger, F. Mayr, J. Deisenhofer, A. Loidl, and T. Kopp, Large and small polaron excitations in  $\text{La}_{2/3}(\text{Sr}/\text{Ca})_{1/3}\text{MnO}_3$  films, *Phys. Rev. B* **69**, 100403(R) (2004).
- [38] Y. Zhang, F. Chen, C. He, L. X. Yang, B. P. Xie, Y. L. Xie, X. H. Chen, M. Fang, M. Arita, K. Shimada, H. Namatame, M. Taniguchi, J. P. Hu, and D. L. Feng, Strong correlations and spin-density-wave phase induced by a massive spectral weight redistribution in  $\alpha$ - $\text{Fe}_{1.06}\text{Te}$ , *Phys. Rev. B* **82**, 165113 (2010).



## Supplementary Material for: Optical properties and carrier localization in the layered phosphide $\text{EuCd}_2\text{P}_2$

C. C. Homes,<sup>1,\*</sup> Z.-C. Wang,<sup>2</sup> K. Fruhling,<sup>2</sup> and F. Tafti<sup>2,†</sup>

<sup>1</sup>*National Synchrotron Light Source II, Brookhaven National Laboratory, Upton, New York 11973, USA*

<sup>2</sup>*Department of Physics, Boston College, Chestnut Hill, Massachusetts 02467, USA*

(Dated: November 10, 2022)

### I. TUTORIAL ON VIBRATIONAL LINE SHAPES

Infrared-active vibrational modes play a dominant role in the optical properties of bad metals and semiconductors due to the either poor or total absence of electronic screening [1]. The optical properties may be described by the Drude-Lorentz model for the dielectric function  $\tilde{\epsilon} = \epsilon_1 + i\epsilon_2$ , described in the main text but repeated here again for convenience,

$$\tilde{\epsilon}(\omega) = \epsilon_\infty - \frac{\omega_{p,D}^2}{\omega^2 + i\omega/\tau_D} + \sum_j \frac{\Omega_j^2}{\omega_j^2 - \omega^2 - i\omega\gamma_j}, \quad (\text{S1})$$

where  $\epsilon_\infty$  is the real part of the dielectric function at high frequency,  $\omega_{p,D}^2 = 4\pi n e^2 / m^*$  is the square of the plasma frequency with carrier concentration  $n$  and effective mass  $m^*$ , and  $1/\tau_D$  is the optical scattering rate for the delocalized (Drude) carriers. In the summation,  $\omega_j$ ,  $\gamma_j$  and  $\Omega_j$  are the position, width, and strength of the  $j$ th vibration or bound excitation, respectively. The complex conductivity is

$$\tilde{\sigma} = \sigma_1 + i\sigma_2 = \frac{2\pi}{Z_0} i\omega [\epsilon_\infty - \tilde{\epsilon}(\omega)], \quad (\text{S2})$$

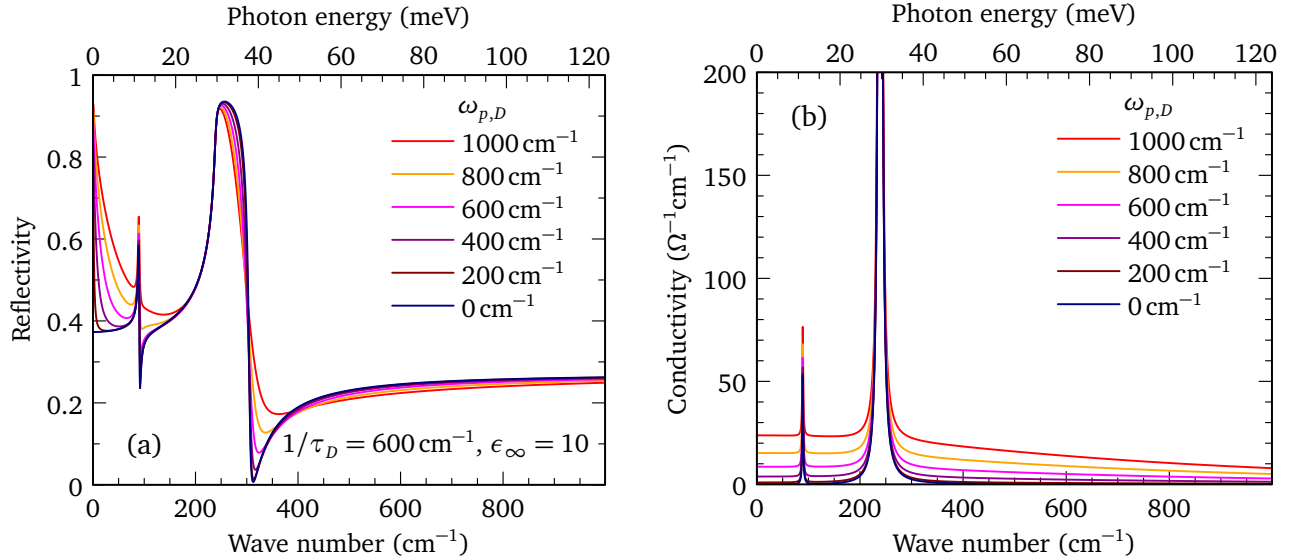


Figure S1. The calculated (a) reflectivity and (b) real part of the optical conductivity for a Drude-Lorentz model with two infrared-active modes, and free-carrier (Drude) component that gradually increases from  $\omega_{p,D} = 0$  to  $1000 \text{ cm}^{-1}$ . The introduction of a weak electronic background has the effect of washing out the deep minima in the line shapes in the reflectivity, while in the optical conductivity the peaks associated with the infrared-active modes retain their amplitude and line shapes, and are simply superimposed upon a weak electronic background of  $\sigma_1 \simeq 20 \text{ } \Omega^{-1} \text{ cm}^{-1}$ .

\* homes@bnl.gov

† fazel.tafti@bc.edu

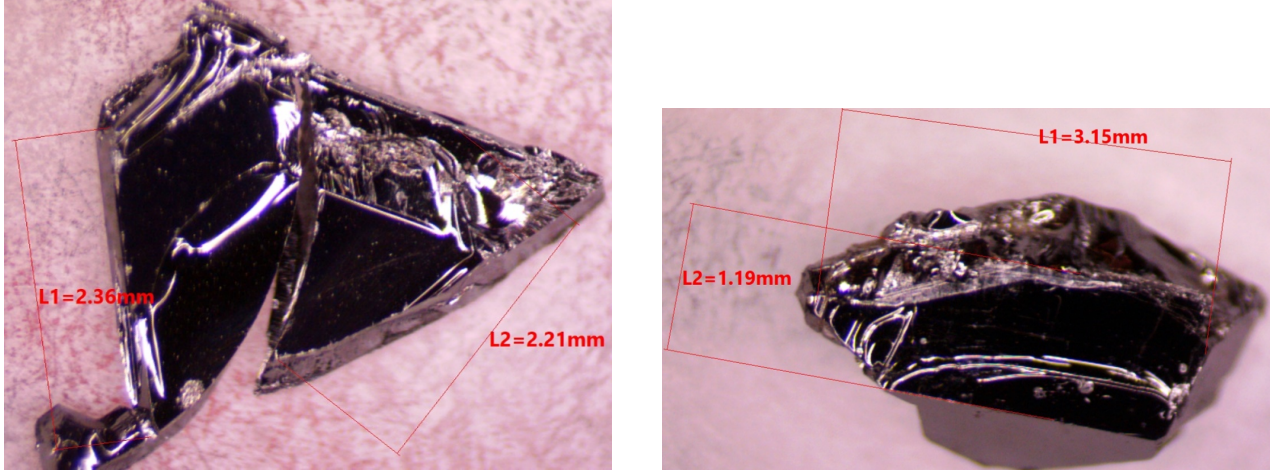


Figure S2. Single crystals of  $\text{EuCd}_2\text{P}_2$  used in the reflectivity experiments. On the left-hand side is a crystal with an  $ab$ -plane  $[(001)]$  surface; this sample actually consists of two pieces; the piece on the left was selected for the in-plane reflectivity experiments. The sample on the right was determined to have an  $a$ - $c$   $[(101)]$  face. Both samples show examples of terraces on the crystals surfaces.

(in units of  $\Omega^{-1}\text{cm}^{-1}$ ), where  $Z_0 = 377 \Omega$  is the impedance of free space. The complex refractive index is  $\tilde{n} = n + ik$ , where

$$n = \left[ \frac{1}{2} \left( \sqrt{\epsilon_1^2 + \epsilon_2^2} + \epsilon_1 \right) \right]^{1/2}, \text{ and } k = \left[ \frac{1}{2} \left( \sqrt{\epsilon_1^2 + \epsilon_2^2} - \epsilon_1 \right) \right]^{1/2}. \quad (\text{S3})$$

The reflectance at a normal angle of incidence is then

$$R = \frac{(n - 1)^2 + k^2}{(n + 1)^2 + k^2}. \quad (\text{S4})$$

To illustrate how even a weak electronic background can introduce large changes to the vibrational line shape in the reflectivity, we will consider two infrared-active modes of similar character to those observed in  $\text{EuCd}_2\text{P}_2$  [see Figs. 4(a) and 4(b) in the main text], with  $\omega_1 = 89$ ,  $\gamma_1 = 2$ , and  $\Omega_1 = 80 \text{ cm}^{-1}$ , and  $\omega_2 = 239$ ,  $\gamma_2 = 5$ , and  $\Omega_2 = 600 \text{ cm}^{-1}$ , with  $\epsilon_\infty = 10$  to reproduce the reflectivity at  $\simeq 1000 \text{ cm}^{-1}$ . Initially, we consider the case of an insulator (semiconductor) in which the free carrier component is completely gapped out ( $\omega_{p,D} = 0$ ). The resulting vibrational line shapes shown in Fig. S1(a) are extremely sharp, dispersive features; in the case of the low-frequency mode, the minima is about  $R \simeq 0.22$ , while for the high-frequency mode,  $R \simeq 0$  at about  $300 \text{ cm}^{-1}$ . As the Drude component is gradually introduced, with  $\omega_{p,D}$  increasing from zero to  $1000 \text{ cm}^{-1}$  in  $200 \text{ cm}^{-1}$  increments, with  $1/\tau_D = 700 \text{ cm}^{-1}$ , the intercept on the ordinate changes immediately from  $R \simeq 0.4$  to unity as soon as  $\omega_{p,D} \neq 0$ ; in addition, the deep minima in the reflectivity associated with the vibrational modes is washed out, so that when  $\omega_{p,D} = 1000 \text{ cm}^{-1}$  it can no longer be observed in the low-frequency mode, and is almost non-existent in the high-frequency mode.

The calculated optical conductivity is shown in Fig. S1(b). For  $\omega_{p,D} = 0$ , the only features present are the two Lorentzian oscillators at  $89$  and  $239 \text{ cm}^{-1}$ ; as non-zero values for  $\omega_{p,D}$  are introduced, a Drude background (a Lorentzian centered at zero frequency with a width of  $1/\tau_D$ ) develops. The infrared modes retain their amplitude and line shape, and are simply superimposed upon this electronic background. This is in stark contrast to the large changes observed in the vibrational line shapes in the reflectivity, illustrating how line shapes can be sensitive probes to small changes in the electronic background.

## II. TERRACING ON THE CRYSTAL FACES

Single crystals of  $\text{EuCd}_2\text{P}_2$  display mirror-like as-grown surfaces, but at the same time may also have steps, or terraces, on the crystal face. This phenomena is shown in crystals in Fig. S2; the sample on the left-hand side of the figure was determined by x-ray diffraction to have an  $ab$ -plane  $[(001)]$  surface. This sample consisted of two pieces; the section on the left was selected for the reflectivity measurements. While the surfaces are of optical quality, there is a prominent step running through the middle of the crystal. The sample shown on the right-hand side of Fig. S2

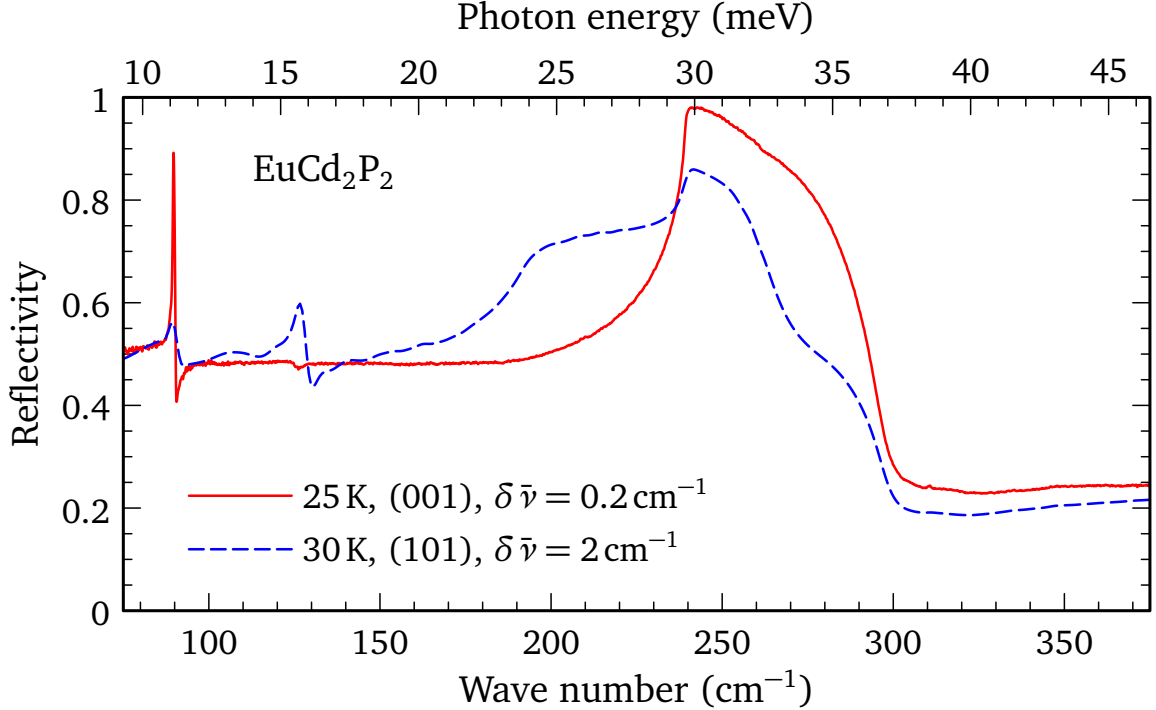


Figure S3. The reflectivity of  $\text{EuCd}_2\text{P}_2$  at 25 K for light polarized in the  $a$ - $b$   $[(001)]$  planes with an instrumental resolution of  $0.2 \text{ cm}^{-1}$  (solid line); the two features due to the  $E_u$  modes are clearly observed at  $\simeq 89$  and  $239 \text{ cm}^{-1}$ , but in addition, there is a weak antiresonance at  $\simeq 126 \text{ cm}^{-1}$ . The reflectivity of a crystal with an  $a$ - $c$   $[(101)]$  face has also been measured at 30 K (dashed line) with an instrumental resolution of  $2 \text{ cm}^{-1}$ ; in addition to the two  $E_u$  modes observed in the in-plane measurements, there are two new features at  $\simeq 126$  and  $206 \text{ cm}^{-1}$ , associated with the  $A_{2u}$  modes active along the  $c$  axis. Note that the low-frequency  $A_{2u}$  mode corresponds precisely with the antiresonance observed in the reflectivity in the  $a$ - $b$  plane measurement.

was determined by x-ray diffraction to have an  $a$ - $c$  face  $[(101)]$  surface. Preliminary measurements on this crystal have been used to estimate the positions of the  $c$ -axis lattice modes that are further discussed in the next section.

### III. C-AXIS CONTRIBUTIONS TO THE A-B PLANE OPTICAL PROPERTIES

The high-resolution ( $0.2 \text{ cm}^{-1}$ ) reflectivity of  $\text{EuCd}_2\text{P}_2$  is shown for light polarized in the  $a$ - $b$  plane in Fig. S3; the two prominent infrared-active  $E_u$  modes are observed at  $\simeq 89$  and  $239 \text{ cm}^{-1}$ . (A simple empirical valence force-field model reproduces the experimental frequencies and intensities. The in-plane atomic displacements of the low-frequency  $E_u$  mode consist of the out-of-phase displacements of the Eu and Cd atoms, with only a minor contribution from the P atoms, which are in phase with the Cd atoms. The high-frequency mode consists mainly of the displacement of P atom, which is out-of-phase to the Cd and Eu atoms.) Superimposed on this result is the reflectivity of the  $a$ - $c$  face with a slightly lower resolution ( $2 \text{ cm}^{-1}$ ) which clearly shows features associated with the  $A_{2u}$   $c$ -axis modes. However, the high-frequency  $A_{2u}$  mode overlaps with the strong  $E_u$  mode, making this reflectivity difficult to fit; it is easier to fit the optical conductivity. The optical conductivity has been determined from a Kramers-Kronig analysis [2] of the reflectivity of the sample with the  $a$ - $c$  face at 30 K by employing a metallic extrapolation at low frequency, and by assuming a constant reflectance above the highest measured frequency point up to  $5 \times 10^4 \text{ cm}^{-1}$ , above which a free-electron approximation is employed [3]. The results for the real and imaginary parts of the optical conductivity of  $\text{EuCd}_2\text{P}_2$  at 30 K are shown in Figs. S4(a) and S4(b), respectively.

The model in Eq. (S1) has been fit simultaneously to the real and imaginary parts of the complex conductivity in the far-infrared region using a non-linear least-squares technique. The conductivity is described by a Drude component as well as four Lorentz oscillators. The results of the fit are shown by the dashed line in Figs. S4(a) and S4(b), respectively, and are summarized in Table I. The low-frequency  $E_u$  mode is observed at  $89.7 \text{ cm}^{-1}$  in the  $a$ - $c$  face, which is almost exactly the value observed in the  $a$ - $b$  planes,  $89.4 \text{ cm}^{-1}$ ; the next two modes at  $\simeq 126.6$  and  $201.6 \text{ cm}^{-1}$  are assigned to the  $c$ -axis  $A_{2u}$  modes. The fit to the weak shoulder at  $\simeq 240 \text{ cm}^{-1}$ , which is the position of the high-frequency  $E_u$

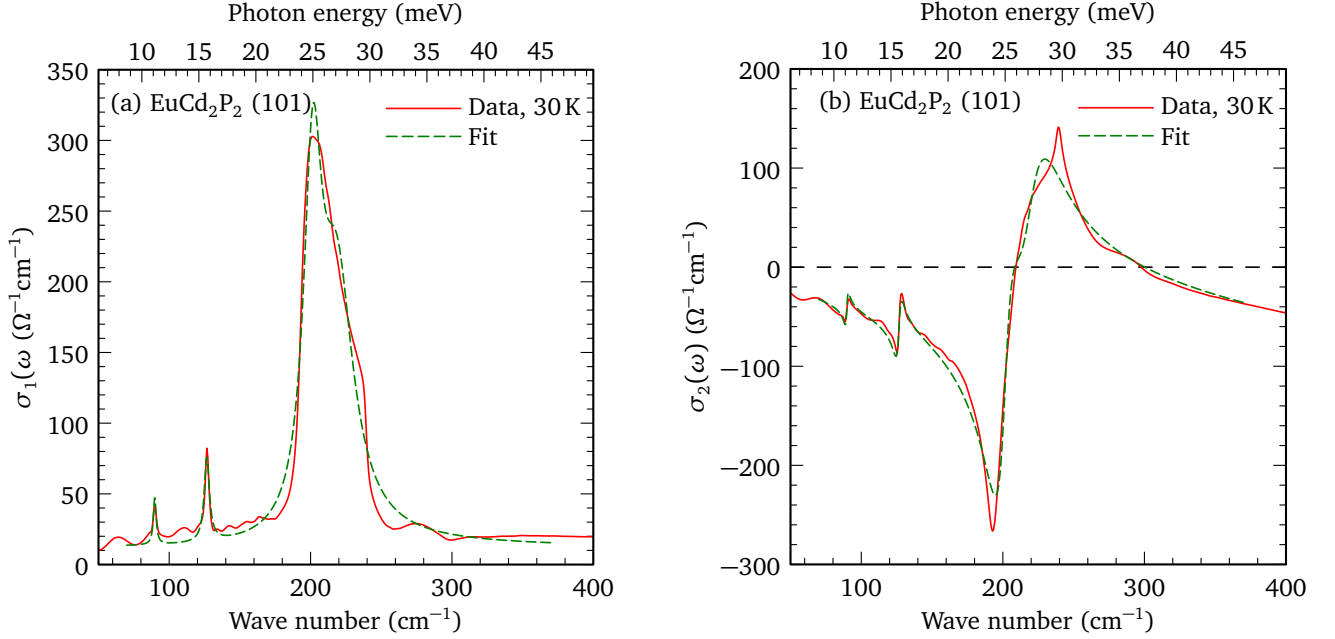


Figure S4. (a) The real part of the optical conductivity for  $\text{EuCd}_2\text{P}_2$  at 30 K for light polarized in an  $a$ - $c$  plane (solid line); the dashed line is the fit to Eq. (S1). (b) The imaginary part of the complex conductivity (solid line) and the fit (dashed line). Note that in both cases the fit to the shoulder in the real part and the peak in the imaginary part of the optical conductivity at  $\simeq 240 \text{ cm}^{-1}$  is rather poor and, where applicable, the line widths are significantly broader than those observed in the  $a$ - $b$  plane conductivity.

mode, is rather poor; in addition, the widths of the two high-frequency modes are considerably larger than the value for the  $E_u$  mode from the  $a$ - $b$  plane measurement with a similar resolution, which suggests that the  $a$ - $c$  face response is more complicated than the simple Drude-Lorentz model being employed here. The fit to the imaginary part of the optical conductivity allows the high-frequency part of the dielectric function to be determined,  $\epsilon_\infty \simeq 12$ . Because the Kramers-Kronig analysis has been performed on a limited frequency range, there is some uncertainty attached to this value.

There are several ways that the  $c$ -axis optical properties may manifest themselves in the  $a$ - $b$  plane response. The first may be a simple mixture of the  $a$ - $b$  plane and  $c$  axis reflectivity. The second may arise from surface misorientations that allow the  $c$  axis longitudinal optic (LO) modes to appear as resonances (antiresonances) in insulating (metallic) systems [4–6]. The position of the LO mode may be estimated from the position and strength of the transverse optic (TO) mode,

$$\omega_{\text{LO}}^2 \simeq \omega_{\text{TO}}^2 + \frac{\Omega_0^2}{\epsilon_\infty}. \quad (\text{S5})$$

The value for the LO mode depends heavily on the value of  $\epsilon_\infty$ . To ensure that the value for  $\epsilon_\infty \simeq 12$  returned from the fits is reasonable, we examine the optical properties in the  $a$ - $b$  plane, where the strong  $E_u$  mode at  $\simeq 239 \text{ cm}^{-1}$  is clearly identified. The temperature dependence of this mode is shown on the left-hand side of Fig. S5 and is indicated by the label “TO”; it should be noted that on this scale the strength of the mode and its symmetric line shape are self evident. The LO mode for this vibration should manifest itself as a peak in the loss function,  $-\text{Im}[1/\tilde{\epsilon}(\omega)]$ , shown on the right-hand side of Fig. S5 and denoted by the label “LO”; peak in the loss function occurs at  $\simeq 296 \text{ cm}^{-1}$  at  $\simeq 15 \text{ K}$  where the background conductivity is reduced due to the more resistive nature of the sample (increasing the background conductivity has the effect of smearing out peak in the loss function). Using these values for the positions of the LO and TO modes, and using  $\Omega_0 \simeq 600 \text{ cm}^{-1}$  from Fig. 4(b), then Eq. (S5) yields  $\epsilon_\infty = 11.8$ , which is very close the value of 12 returned from the fit, validating the earlier result and suggesting that  $\epsilon_\infty$  likely has little in the way of any asymmetry.

Using the fitted values for the TO modes in Fig. S4 and  $\epsilon_\infty = 12$ , the estimated values for the LO modes are listed in Table I. The fact that the antiresonance in Fig. S3 occurs at exactly the same frequency as the peak in the optical conductivity,  $126.6 \pm 0.8 \text{ cm}^{-1}$ , implies that it is associated with the  $c$ -axis  $A_{2u}$  TO mode rather than the LO mode, estimated to be occur at  $\simeq 131.7 \text{ cm}^{-1}$  indicating that the  $c$ -axis contamination arises simply from the mixing of the  $a$ - $b$  plane and  $c$  axis reflectivities due to the presence of  $c$ -axis steps, or terraces, in the  $a$ - $b$  plane face.

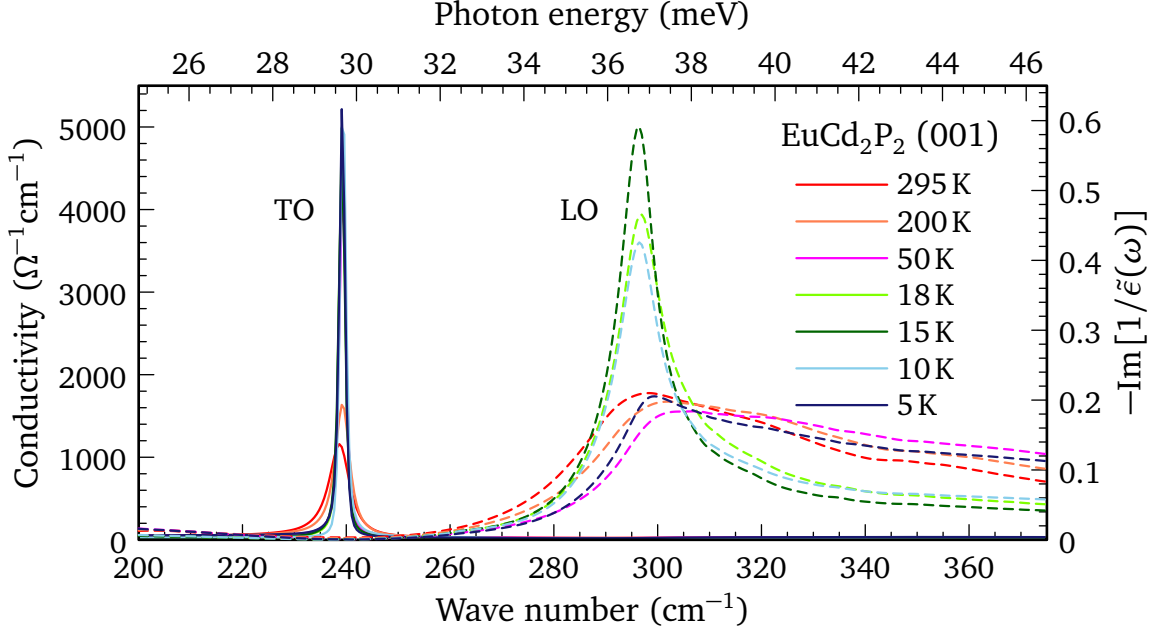


Figure S5. The temperature dependence of the optical conductivity (solid lines, left axis) and the loss function (dashed lines, right axis) for the strong  $E_u$  mode in  $\text{EuCd}_2\text{P}_2$  for light polarized in the  $a$ - $b$  [(001)] plane. The TO mode is very strong and narrow, with the maximum observed at  $\simeq 239 \text{ cm}^{-1}$ , while the LO mode is broader with a maximum of  $\simeq 296 \text{ cm}^{-1}$  at about 15 K where the resistivity in the sample is close to its maximum (increasing the electronic background has the effect of smearing out the loss function in the region of the LO mode).

Table I. The parameters for the Drude-Lorentz model fitted to the real and imaginary parts of the optical conductivity  $\text{EuCd}_2\text{P}_2$  at 30 K light polarized in an  $a$ - $c$  plane. The Drude values are  $\omega_{p,D} \simeq 1468 \text{ cm}^{-1}$  and  $1/\tau_D \simeq 1070 \text{ cm}^{-1}$ . All values are in units of  $\text{cm}^{-1}$ , unless otherwise indicated.<sup>a</sup>

| Mode     | $\omega_{\text{TO},j}$ | $\omega_{\text{LO},j}$ | $\gamma_j$ | $\Omega_j$ |
|----------|------------------------|------------------------|------------|------------|
| $E_u$    | 89.7                   | 91.9                   | 2.4        | 69         |
| $A_{2u}$ | 126.6                  | 131.7                  | 4.5        | 126        |
| $A_{2u}$ | 201.6                  | 245.2                  | 15.8       | 484        |
| $E_u$    | 218.9                  | 269.7                  | 28.1       | 541        |

<sup>a</sup>  $\epsilon_\infty = 12$ .

- 
- [1] C. C. Homes, A. W. McConnell, B. P. Clayman, D. A. Bonn, R. Liang, W. N. Hardy, M. Inoue, H. Negishi, P. Fournier, and R. L. Greene, Phonon Screening in High-Temperature Superconductors, *Phys. Rev. Lett.* **84**, 5391 (2000).
- [2] M. Dressel and G. Grüner, *Electrodynamics of Solids* (Cambridge University Press, Cambridge, 2001).
- [3] F. Wooten, *Optical Properties of Solids* (Academic Press, New York, 1972) pp. 244–250.
- [4] D. W. Berreman, Resonant Reflectance Anomalies: Effect of Shapes of Surface Irregularities, *Phys. Rev. B* **1**, 381 (1970).
- [5] M. Reedyk and T. Timusk, Evidence for  $a$ - $b$ -plane coupling to longitudinal  $c$ -axis phonons in high- $T_c$  superconductors, *Phys. Rev. Lett.* **69**, 2705 (1992).
- [6] C. C. Homes, J. M. Tranquada, and D. J. Buttrey, Stripe order and vibrational properties of  $\text{La}_2\text{NiO}_{4+\delta}$  for  $\delta = 2/15$ : Measurements and *ab initio* calculations, *Phys. Rev. B* **75**, 045128 (2007).